EXPERIMENTS ON STRUCTURALLY MISTUNED UHBR OPEN-TEST-CASE FAN ECL5/CATANA

Christoph Brandstetter, Alexandra P Schneider, Anne-Lise Fiquet, Benoit Paoletti, Xavier Ottavy

EXPERIMENTS ON STRUCTURALLY MISTUNED UHBR OPEN-TEST-CASE FAN ECL5/CATANA

Christoph Brandstetter[1,*], Alexandra P. Schneider[1], Anne-Lise Fiquet[1], Benoit Paoletti[1], Xavier Ottavy[1],

[1]Univ. Lyon, École Centrale de Lyon, CNRS, Univ. Claude Bernard Lyon 1, INSA Lyon, LMFA, UMR5509, 69130, Écully, France

ABSTRACT

The operational capabilities of turbofan engines encounter limitations due to instabilities arising from tightly coupled interactions among aerodynamics, acoustics, and structural mechanics. Modern fans and compressors exhibit Non-Synchronous Vibration (NSV), leading to safety-critical blade oscillations. In contrast to self-excited phenomena such as flutter, NSV stems from the convection of aerodynamic disturbances that synchronize with blade eigenmodes. Understanding this phenomenon is challenging, as its intricate interaction patterns and the occurrence of flow separations constrain the predictive capabilities of current state-of-the-art methods.

To establish a comprehensive benchmark dataset on the aeroelastic behavior of modern Ultra-High Bypass Ratio (UHBR) architectures, the European CleanSky-2 project CATANA aimed to examine a carbon composite fan stage, ECL5, utilizing multi-physical instrumentation. Recently, experiments on a structurally tuned reference configuration were conducted, revealing high-amplitude Non-Synchronous Vibration (NSV) at multiple subsonic speedlines. The observed interaction modes and instability onset differed significantly from numerical predictions using both LRANS and URANS with prescribed harmonic blade motion.

In an effort to enhance the dataset, two additional fan configurations with identical blade profile geometries were investigated: one featured a structurally mistuned rotor with approximately doubled frequency variation of all eigenmodes compared to the reference, and the other involved a case with locally increased tip clearance on individual blades.

This paper presents the experimental results of a sensitivity study and explores the influence of structural mistuning and tip clearance variation associated with manufacturing tolerances.

Contrary to the intended outcome, it will be demonstrated that the mistuned case exhibited higher blade vibration amplitudes than the reference case during NSV. Detailed instrumentation reveals that the mistuning pattern was effectively transferred to the rotating system, but aerodynamic mistuning, particularly concerning tip clearance, emerged as a dominant factor. The non-synchronous forced-response nature of NSV during highly throttled operation ultimately dictates the observed response levels under different conditions, necessitating a thorough analysis to evaluate the robustness of a specific configuration.

These results contribute valuable insights to the open dataset for the ECL5 configuration, benefiting the research community. Particularly noteworthy is the detailed capture of blade-to-blade variations in this research, which will prove instrumental in validating numerical methods.

Keywords: Low-speed fan, Non-synchronous vibration

*Corresponding author: christoph.brandstetter@ec-lyon.fr

NOMENCLATURE

Acronyms

EO	Engine Order
FEM	Finite Element Method
FSI	Fluid-Structure Interaction
IBPA	Inter Blade Phase angle
LE	Leading Edge
LES	Large Eddy Simulation
LCO	Limit Cycle of Oscillations
LRANS	Linearized RANS
MC	Mid-Chord
NSV	Non-Synchronous Vibration
OGV	Outlet Guide Vane
RANS	Reynolds-Averaged Navier-Stokes
SDOF	Single-Degree-Of-Freedom
TE	Trailing Edge
TT	Tip-timing
TCS	Turbulence Control Screen
UHBR	Ultra-High-Bypass-Ratio
URANS	Unsteady RANS

Notations

N_v	Nodal diameter $[-]$
N_a	Aerodynamic wave number $[-]$
P_s	Static pressure $[bar]$
P_t	Total pressure $[bar]$
T_t	Total temperature $[K]$
C_{ax}	Axial chord $[-]$
f	Frequency $[Hz]$
dx	Axial displacement $[mm]$
dr	Radial displacement $[mm]$
P_{atmo}	Atmospheric pressure $[bar]$
ε	Strain $[\mu m/m]$
ε_{M_j}	Scope limit of Mode-j $[\mu m/m]$
Π_t	Total pressure ratio $[-]$
$\dot{m}_{std}$	Standard mass-flow rate $[kg/s]$
$rd\theta$	Tangential displacement $[mm]$

ω	Angular frequency $[rad/s]$
Ω	Angular velocity $[rad/s]$
ΔP_s	Non-synchronous pressure fluctuation $[bar]$

Superscripts and subscripts

$\cdot^S$	Stationary frame of reference
$\cdot^R$	Rotating frame of reference
$\cdot_a$	Aerodynamic Mode
$\cdot_v$	Structural Mode
$\cdot_r$	Rotor
$\cdot_{PS}$	Pressure side
$\cdot_{SS}$	Suction side
$\hat{\cdot}$	Fourier coefficient
$\bar{\cdot}$	Temporal average

INTRODUCTION

Modern turbofan architectures often encounter limitations in stability due to interactions among aerodynamic, aeroelastic, and aeroacoustic phenomena. Extensive research has successfully addressed aerodynamic instabilities and the shift of the aerodynamic stability limit. Similarly, self-excited aeroelastic instability, known as flutter, has been a focal point of recent research initiatives, such as in the European project CA3VIAR (GA 864256). The interaction of trapped acoustic modes in the machine intake with torsional blade modes has been identified as the primary physical driver for fan flutter [1]. Understanding this coupling phenomenon has led to the development of predictive simulation methods and countermeasures, including reducing the torsion component in blade eigenmodes [2–4] and introducing frequency mistuning [5, 6].

However, the emergence of non-synchronous blade vibration (NSV)[7] at near stall conditions has raised significant safety concerns, occurring in numerous academic [8, 9] and industrial [10, 11] configurations that were aerodynamically optimized.

Studies from the past decade have revealed that NSV in compressors and low-speed fans results from the propagation of aerodynamic disturbances close to the casing, synchronizing with structural blade eigenmodes, distinguishing it from flutter [12].

Understanding these highly interdependent fluid-structure instabilities is crucial, especially in the context of future Ultra-High-Bypass-Ratio (UHBR) concepts. The challenge lies in the predictability of current aeroelastic methods when applied to the innovative generation of low-speed fans. These fans feature geometric characteristics such as low hub-to-tip ratios, broad midspan and tip chords, and sharp leading edges at high channel heights. While optimized for low-transonic performance, they are sensitive to flow separation at subsonic operation and are characteristic of machines that experience part-speed NSV. This presents significant challenges for predictive numerical methods in these architectures:

1. Accurate simulation: Precise simulation of passage blockage and disturbance propagation near the casing is necessary, along with capturing flow separation at the blade leading edges, which exhibits a non-linear dependency on oscillation amplitude.

2. Lock-in occurrence: Lock-in is commonly observed for substantial blade vibration amplitudes, necessitating robust mesh deformation techniques.

3. Full-annulus simulations: Full-annulus simulations are essential to avoid constrained circumferential wave-numbers.

4. Prescribed harmonic blade motion: The use of prescribed harmonic blade motion can overly constrain the coupled system, resulting in non-convergent periodic behavior and hindering the derivation of system stability [13].

The current state-of-the-art NSV fan or compressor simulation, featuring a full-annulus URANS setup with a stage intake and a choked nozzle, accommodates geometric blade inhomogeneity concerning tip clearance or stagger with only minor additional effort.

As demonstrated in this paper, even an intentionally tuned fan can exhibit significant blade-to-blade variation due to manufacturing tolerances, impacting the coupled system behavior and potentially dominating the aerodynamic coupling driving NSV.

With the general goal of characterizing NSV in modern UHBR fan designs, the 16-bladed open-test-case ECL5 was designed and tested in the CATANA project. A set of 48 blades was fabricated to achieve a maximum number of geometrically and structurally identical blades. The reference configuration (CATREF) and the mistuned case (CATMIS) were selected based on ping-tests to determine the eigenfrequency of the first three blade modes. To account for geometric variation, all blades were measured in a 3D-scanner, allowing determination of local tip clearance and stagger angle.

As non-negligible variations of tip clearance were observed in the experiment, an additional blade-set was assembled based on the mistuned case, but with three shortened blades (CATSRT). Advanced techniques were employed to measure aerodynamic disturbances interacting with blade vibrations. The instrumentation suite is robust, enabling a clear characterization of aeroelastic interaction and a meticulous examination of system symmetry.

The three configurations were tested within a 6-month period, repeatedly probing the stability limit at different speedlines to answer the following research questions:

1. How does the imposed mistuning affect the global system behavior in terms of aerodynamic performance, forced response, and the evolution of NSV at part speed?

2. Can the observed interaction modes during NSV be associated with the (cold) blade properties?

3. What are the dominant features that need to be considered to design a successful mistuning pattern?

4. Does the current understanding of the convective NSV mechanism need to be revised?

While aligning with established theoretical trends, the experiments reveal notable disparities in critical modes and propagation speeds, highlighting significant asymmetry even in the tuned CATREF configuration. The results clarify that the tested configurations, intended to exhibit a significant variation in system symmetry, converge concerning aeroelastic behavior when geometric variation is considered.

The investigation extends beyond observing aeroelastic behavior, exploring aerodynamics in the presence of geometric variations. The analysis allows for rigorous comparisons with numerical simulations and illuminates the challenges faced in achieving accurate predictions. The carbon fibre UHBR configuration has inherently different characteristics compared to known open test

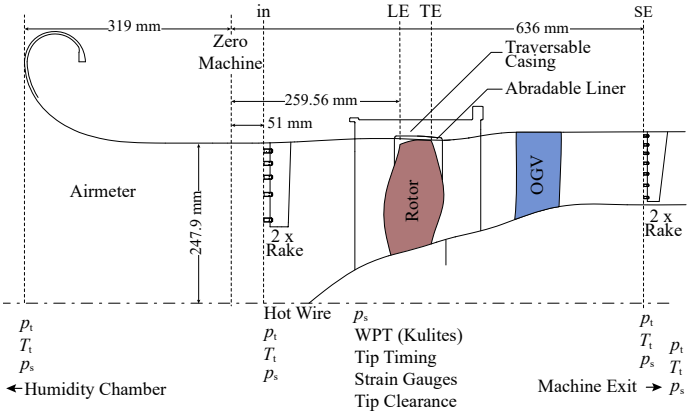

FIGURE 1: Schematic view of the machine core and probe positions

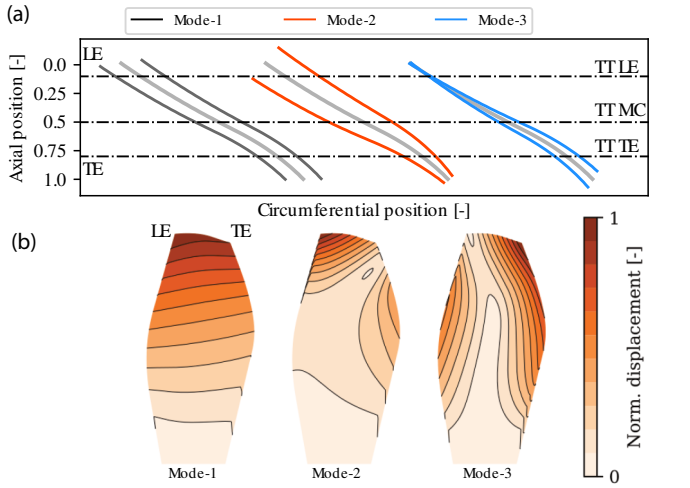

FIGURE 2: a) Tip deflection at design speed for Mode-1, Mode-2 and Mode-3 (N_v=0) and axial position of tip-timing sensors. Amplitude represents 400% scope limit at design speed. b) Normalized displacement map for all modes

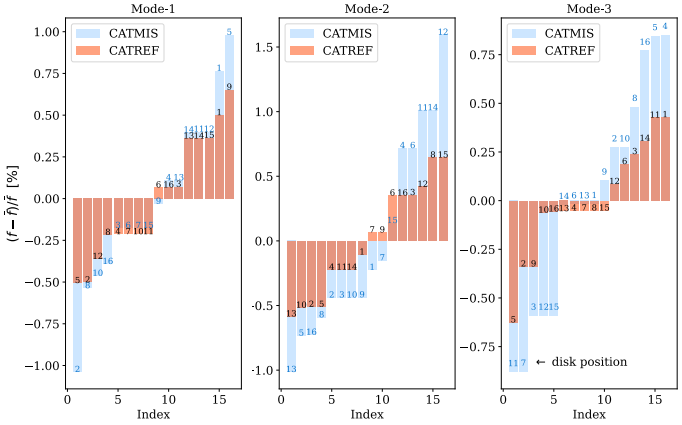

FIGURE 3: Blade eigenfrequencies for Mode-1, Mode-2 and Mode-3 for the tuned reference rotor (CATREF) and the mistuned rotor (CATMIS) from ping-test

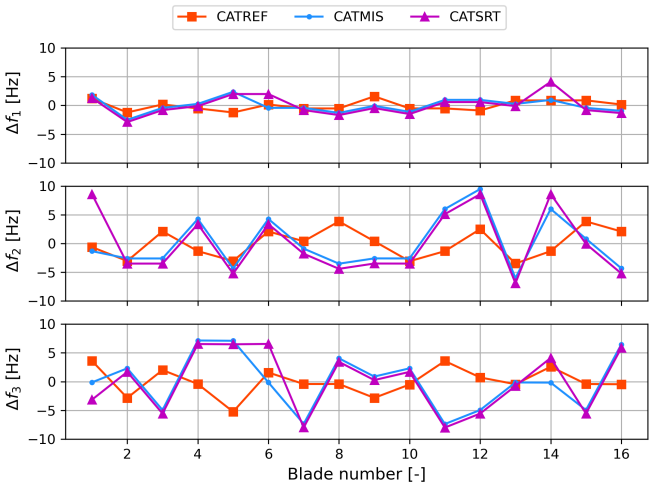

FIGURE 4: Assembled ping-test eigenfrequency patterns for all tested configurations

cases (NASA Rotors 37/67 [14, 15], TUDa [16]). Collectively, these experiments, coupled with the shared geometry and mechanical properties of the open-test-case, constitute a benchmark dataset for turbomachine aerodynamics and aeroelastics. They possess potential for validating simulations near the stability limits and provide insights into diverse instability-causing phenomena, ultimately proving crucial for future composite architectures.

EXPERIMENTAL SETUP AND METHODS

Open-test-case fan

The open-test-case fan stage, created at Ecole Centrale de Lyon, features 16 carbon-fiber rotor blades and 31 aluminum OGVs, schematically shown in Fig. 1. At 11000rpm, the aerodynamic design point was targeted at a standard mass flow rate of 36.0kg/s with a relative tip Mach number of 1.

The fan stage exhibits a total pressure ratio of 1.35 and an isentropic efficiency of 92%. Within the project CATANA, a total of 48 blades was manufactured from pre-impregnated carbon fiber layers, employing a specific process described in [17].

Post-fabrication, each blade was controlled in a 3D-scanner and frequency response based on ping-tests. This process determined their static moment and mass, allowing for careful selection to form different rotor assemblies.

TABLE 1: Average Ping-test (0% speed) eigenfrequencies

Configuration	f_1 [Hz]	f_2 [Hz]	f_3 [Hz]
CATREF	242.5	595.5	838.1
CATMIS	241.0	593.4	838.4
CATSRT	241.4	594.3	838.7

Selection of mistuning pattern

The selection for the tested configurations was based on the ping test results from a shaker setup with foot-point excitation and resonant spectra measured using a laser-interferometer. Blades were clamped in a block with calibrated pistons simulating the centrifugal force under rotation. Repeated conduction of those

tests ensured robustness of the procedure to determine the 'cold' blade properties [1]. The measured eigenfrequencies for the first 3 modes are presented in table 1 and their respective tip deflections and mode shapes at design speed are illustrated in Fig. 2. For the reference configuration CATREF, the blades were directly selected by choosing those which provide the minimum variation for all 3 modes. The assembly pattern was designed by selecting opposite pairs of blades with equal static moment to reduce balancing issues.

In the experiments with the selected reference configuration all 3 modes proved sensitive to limit-cycle NSV [18], which was in contrast to the numerical predictions [13, 19]. For Mode-1 and Mode-2 the experiments showed inconclusive wave-number decompositions at 80% rotor speed, but Mode-3 revealed a clearly depicted assembly mode of N_v3 interacting with a backward traveling wave of 13 lobes, reaching significant vibration amplitudes. Determination of the propagation speed of the aerodynamic showed an average value of 57%. With these results, the authors aimed to design a blade assembly to reduce vibration amplitude of Mode-3 by disturbing the resonance of the coupled system. It is well known that the impact of mistuning on the stability of the cyclically coupled system will depend on the specific relationships between the mistuning and the coupling strengths. Small mistuning might have a stabilizing effect by disrupting resonance, while large mistuning might lead to a more destabilized system, especially if it introduces new resonance conditions. Moderate mistuning may have complex effects that depend on the specific characteristics of the system. The design space for the experiments was limited by the manufactured blades, whose eigenfrequency distribution was lower than expected before fabrication.

The theory behind the design of the selected mistuning pattern was based on the reduced order model provided in [20]. The authors proposed SDOF oscillators coupled by a term that considers the constant convection speed of aerodynamic disturbances. The disturbance term is locally generated by oscillating blades, propagated and causes modal forcing on remote blades. Phase and amplitude of disturbance generation and modal forcing is calibrated by CFD simulations with harmonic oscillation of an individual blade. Blade individual stiffness from the ping tests and the propagation speed of disturbances measured with the reference configuration was considered in the time-marching formulation of the model, described in [12]. Forcing coefficients were based on a CFD calculation for an operating point close to onset of NSV (24.5 kg/s). For the 32 blades that were available for the mistuned configuration CATMIS, all possible assembly patterns with blades of equal static moment in opposing disk position were simulated. For the best pattern the results indicated a slight improvement of stability by reducing negative aerodamping of the coupled system by approximately 20%. This theoretical improvement was considered small, but sufficiently significant to be measured in experiments.

Fig. 3 presents the sorted eigenfrequency distribution with the respective disk positions. This illustration emphasizes the spreading of the eigenfrequencies, with CATMIS providing an approximately doubled variation for Mode-2 and Mode-3.

To investigate the influence of individual blades, a third configuration based on CATMIS with increased tip clearance on 3 distinct blades was designed using shortened blades on disk position 1, 6 and 14 (CATSRT). Its stability was predicted similar to the mistuned case by the reduced order model. The assembled patterns are illustrated in Fig. 4 showing the eigenfrequency distributions in Hz for the first 3 modes relative to the assembly average indicated in table 1. Individual blade characteristics (tip clearance and blade eigenfrequencies) of each configuration are presented in the appendix A.

Experimental Methods

The three presented configurations have been experimentally tested at the open cycle test facility Phare-2 at Ecole Centrale de Lyon, driven by an electrical motor with a maximal power of 3MW [21]. A turbulence control screen (TCS) is installed in front of the machine to provide homogeneous inflow conditions [22]. The instrumentation employed to derive the fan stage performance is depicted in Fig. 1. Two rakes are installed in the machine intake (plane in) and two extra rakes are positioned downstream of the OGVs (plane SE), equally distributed around the circumference (180°). For operability measurements, this instrumentation is removed, only non-intrusive instrumentation remains.

To characterize the mechanical behavior of the rotor, two blade vibration measurement systems have been applied:

Blade vibration in the rotating frame of reference has been measured using blade-mounted strain gauges on each blade suction side. In addition, half of the number of blades have been instrumented by a second strain gauge at the pressure side, as detailed in [18].

Tip clearance and individual blade deflection in the stationary frame of reference are captured using a tip-timing (TT) system [23], enabling the characterization of assembly modes. For the reference rotor, a total of six calibrated probes have been integrated in the casing wall: two near the leading edge at $11\%C_{ax}$ (TT LE), three at mid-chord $64\%C_{ax}$ (TT MC) and only one near the trailing edge $88\%C_{ax}$ (TT TE). An extra probe at the trailing edge is added for the CATMIS and CATSRT configurations to improve the detection of Mode-3 which has a high torsional component at the blade trailing edge, as shown in Fig. 2.

Characterization of traveling aerodynamic and structural modes

Throughout this paper, conventional windowed Fourier transformation is used to investigate spectral content of aerodynamic and structural signals [24]. To determine wave characteristics of propagating aerodynamic patterns and structural assembly modes, the method of pairwise cross-correlations with circumferentially distributed sensors is used [25]. The cross correlation between two unsteady signals (s) is given as:

$$s_1 \star s_2(j) = \frac{1}{I}\frac{1}{\sigma(s_1)\sigma(s_2)}\sum_{i=0}^{I-j-1} s_1(i)s_2(i+j) \qquad (1)$$

with i indicating the sample and I the samples per revolution, σ the respective standard deviation of the signals to normalize

[1] Reports of Composite AeroelasTics ANd Aeroacoustics project H2020

the correlation value. The correlation vector can be mapped to a circumferential propagation speed $\frac{\Omega}{\Omega_r}$ using the sensor spacing $\Delta\Theta_{12}$:

$$\frac{\Omega}{\Omega_r} = \frac{\Delta\Theta_{12}/360°}{j/I} \tag{2}$$

With the signal frequency ω_a known from Fourier transformation, wave number N_a of an aerodynamic mode (or for a structural Mode N_v, ω_v and Ω_v) can be derived as:

$$N_a = \frac{\omega_a}{\Omega_a} \tag{3}$$

For a structural nodal diameter N_v of the fan, the inter-blade phase angle σ_v (IBPA) is derived as:

$$\sigma_v = \frac{2\pi N_v}{N_b} \tag{4}$$

As will be seen in the analysis section, the fans do not oscillate with constant IBPA, even if coherent assembly patterns (N_v) are observed. Presented values of IBPA are scaled to match the unit of a nodal diameter according to Eq. 4.

RESULTS

Aerodynamic performance

The fan stage performance was determined through experimental rake traverses conducted at the stage inlet and exit under varying rotational speeds and multiple stable operating conditions.

Fig. 5 (a, b) illustrates the fan stage's total pressure ratio and isentropic efficiency for both 80% speed (subsonic conditions) and the design speed (transonic conditions), denoted as N80 and N100 respectively, for all rotor assemblies. The aerodynamic design point of the machine is marked as DP in the figure, corresponding to a mass flow rate of 36 kg/s at design speed almost coincident with the measured isentropic peak efficiency operating point (PE). Additionally, the peak pressure operating point (PP) was observed at a mass flow rate of 32 kg/s, demonstrating a large operating range where the fan stage maintains an isentropic efficiency above 85% at design speed.

The stage total pressure ratio of both CATMIS and CATSRT configurations reached higher values at design speed compared to the CATREF, with a maximum difference of 0.45% observed at PE. This trend persisted at 80% speed, where CATMIS and CATSRT configurations exhibited identical performance with higher total pressure ratios and isentropic efficiencies at PE compared to CATREF. This performance difference between configurations exceeds the measurement uncertainty [26] and was observed during repeated experiments.

For all rotor configurations, throttling the rotor towards lower massflow rate resulted in the emergence of non-synchronous vibrations (NSV) and the abortion of experiments before the onset of rotating stall at all subsonic speedlines. Experiments were stopped when strain gauge values indicated 50% of the Goodman scope limit. At transonic speedlines (100% - 105%), the stable operating range was constrained by the onset of rotating stall towards low massflow rates [18].

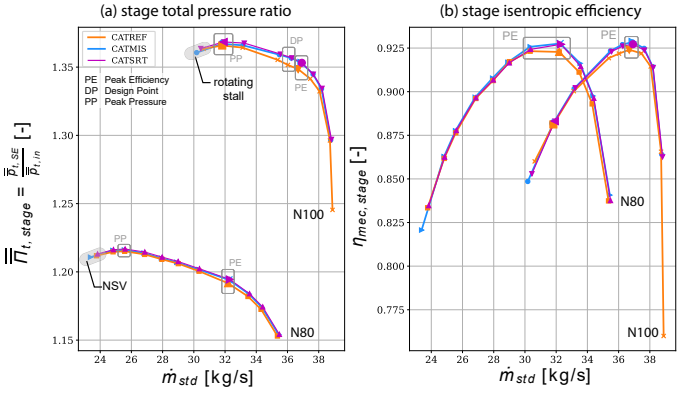

FIGURE 5: Fan stage characteristics for CATREF, CATMIS and CATSRT configurations from experiments: total pressure ratio (a) and isentropic efficiency (b).

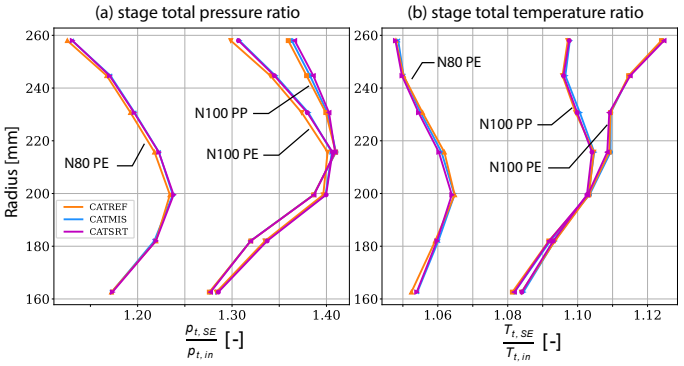

FIGURE 6: Radial profiles downstream the OGV at PE at 80% speed and PE, PP at 100% of design speed: total pressure ratio (a) and total temperature ratio (b).

To further investigate the overall aerodynamic behavior, Fig. 6 presents the radial evolution of total pressure ratio and total temperature ratio downstream of the OGV at PE and PP operating conditions at design speed, as well as at PE conditions at 80% speed. All configurations displayed mostly similar radial profiles for total pressure and temperature ratios. In accordance with Fig. 5, the radial profiles for total pressure ratio exhibited minor advantages for the mistuned configurations, primarily located from mid-span towards the casing. The associated total temperature ratio shows neglibile variations.

These results reveal substantial similarity among the three configurations, indicating comparable work input under specified operating conditions. Higher pressure ratio over a broad channel height range for CATMIS and CATSRT suggests a modified loss mechanism. As the profile evolution towards the hub and casing remains consistent, corner separation issues in the OGV can be ruled out. Since the OGV has not undergone changes or disassembly between measurements, the most probable reason for the reduced performance of the reference configuration is considered to be related to high-span aerodynamics in the fan. This could involve shock-boundary-layer interactions or blockage issues associated with the tip-leakage flow and will be subject of further research.

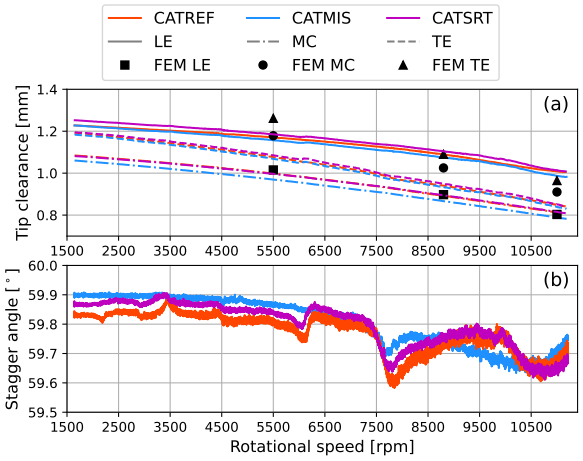

FIGURE 7: (a) Evolution of the average tip clearance as function of the rotational speed at different axial positions: LE leading edge (11%C_{ax}), MC mid-chord (64%C_{ax}) and TE trailing edge (88%C_{ax}) with FEM prediction and (b) and evolution of the stagger angle with rotational speed for CATREF, CATMIS and CATSRT configurations.

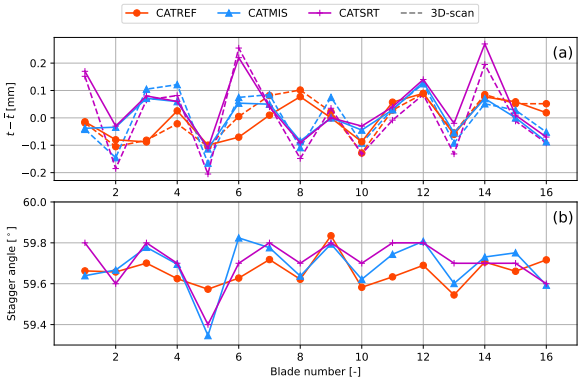

FIGURE 8: Blade-to-blade variation of measured leading edge tip clearance with 3D-scan results (a) and stagger angle (b) at design condition (DP) for CATREF, CATMIS and CATSRT configurations.

Structure identification at stable operation

To identify structural characteristics of each configuration under rotation, an acceleration was conducted from 1600 rpm to 11200 rpm at a constant ramp rate of 50 rpm/s with a throttle setting corresponding to design point at 100% speed.

Fig. 7(a) presents the measured tip clearance. The plotted curves depict the average values of all blades at Leading Edge (LE) (11% C_{ax}), Mid-Chord (MC) (62% C_{ax}), and Trailing Edge (TE) (88% C_{ax}). For all configurations, a consistent reduction in mean tip clearance is evident with increasing rotational speed. The experimental reduction in tip clearance from 50% to 100% of the design speed at mid-chord is approximately 0.18 mm, corresponding to 15% of the cold tip clearance at this position. The reduction at the LE is marginally lower, while at the TE, it is higher due to blade untwist.

The tip timing system allows for the determination of the stagger angle by comparing the arrival time of the blades at leading-edge and trailing edge positions (compare Fig. 2) for each blade. The resulting graphs for the acceleration at constant throttle setting the measured values are shown in Fig. 7(b). The general trend of decreasing stagger angle over rotation speed is similar for all blades, with an overall change of 0.3 degrees over the speed-range. Average values are very close for all configurations (<0.1deg difference), but resonant crossings are observed. As will be seen in Fig. 9, one main crossing occurs at 7700 rpm that leads to blade oscillation in the first eigenmode. Obviously, the algorithm to detect the local stagger angle is not robust to this and measured stagger variations near resonant crossings must be considered accordingly, but minor difference between configurations is evident.

Blade-to-blade variation of the tip clearance exceeds the expected manufacturing goals. Fig. 8(a) shows the measured tip clearance at design point for 100% speed at the leading edge. For the reference configuration, individual blades show values 0.1mm larger or smaller than the average. The same applies for the CATMIS setup, with identical average value. The plot for CATSRT illustrates the 3 shortened blades at position 1, 6 and 14, which provide a local increase of more than 0.2 mm in tip clearance compared to the average. In addition to the capacitive measurements, the results from 3D-scans of the individual blades are presented for the leading edge position. Within an uncertainty of 0.05mm, the presented curves are identical to the assembly measurements under rotation, indicating adequate transferability.

For peak efficiency throttle condition at 100% speed, the graph in Fig. 8(b) illustrates the bladewise distribution of stagger angle. All blades except for blade 5 in the mistuned configurations are well staggered at the tip within a range of ±0.12 degrees. Blade 5 (CATMIS/CATSRT) presents a decreased stagger angle of −0.3 degrees with respect to the assembly average. This distribution could not be derived from the 3D scans which indicated a cold stagger variation of less than ± 0.1 degrees (including blade 5 of CATMIS/CATSRT), in a pattern which was not coincident with the rotating experiment. Hence the static untwist of the blades under rotation increases asymmetry of the assembly for all measured configurations, in average by 20% for peak efficiency condition.

Fig. 9 illustrates the Campbell diagrams for CATREF (a) and CATMIS (b) rotors, derived from strain gauge signals averaged across all blades. To enhance forced response for mode identification, the experiments were conducted without the turbulence control screen [22].

The EO-crossings, highlighted by black circles derived from tip-timing data scaled to the Goodman limit, are featured. Notably, the strain gauge amplitude is not scaled to the Goodman limit, as this determination is only feasible for discrete modal frequencies [24]. Dashed lines represent the FEM prediction of blade eigenfrequencies for the first three modes. The Campbell diagram of the CATSRT rotor mirrors that of the CATMIS configuration and is excluded.

Both configurations demonstrate similar behavior, particularly a substantial resonance between Mode-1 and EO2 within a broad range around 7700 rpm. This resonance reaches a scope limit of 42% for CATREF based on tip-timing data and approximately 48% for CATMIS. The M1/EO3 and M1/EO4 crossings indicate amplitudes lower than 10% of the scope limit for

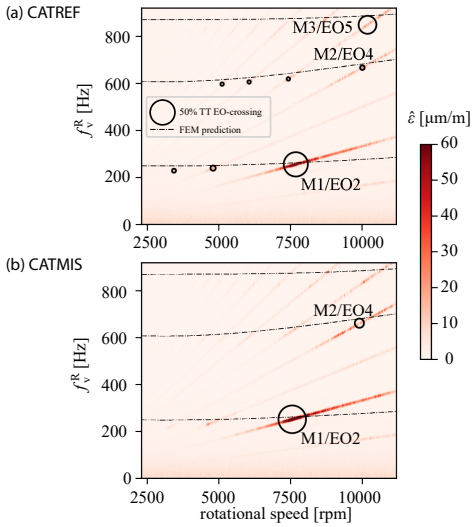

FIGURE 9: Campbell diagrams from averaged strain gauges signal, tip-timing data at EO-crossings with FEM prediction of blade eigenfrequencies for Mode-1, Mode-2 and Mode-3 for CATREF (a) and CATMIS (b) configurations.

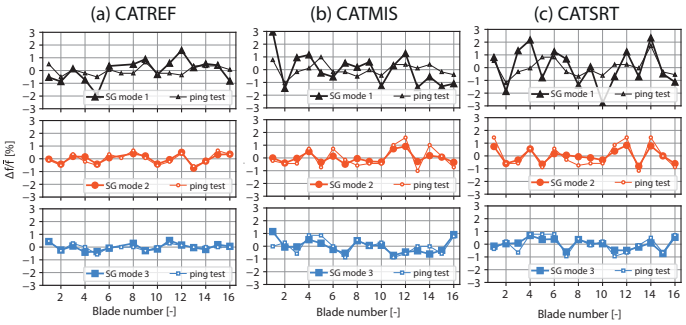

FIGURE 10: Blade eigenfrequencies variation from strain gauge signals at the onset of NSV for CATREF (24.3 kg/s), CATMIS (24.1 kg/s) and CATSRT (24.3 kg/s) configurations and from ping-test . Strain gauge on blade 7 was lost during the experiments for the CATREF rotor (a).

CATREF. In contrast, the CATMIS rotor exhibits comparable amplitudes from strain gauge signals, but precise identification based on tip-timing data remains elusive.

The dominant crossing of Mode-2 is observed at 10000 rpm with EO4 for both rotors, resulting in a scope limit of 8% for CATREF and approximately 16% for CATMIS. The M3/EO5 crossing, observed at 10190 rpm in both Campbell diagrams, exhibits an amplitude of 31% of the scope limit for CATREF, while clear identification of this crossing was not possible for the CATMIS rotor with the tip-timing system.

Regarding the FEM prediction, the blade eigenfrequencies slightly surpass those of the manufactured blades across the entire speed range, with a maximum difference of 4% for Mode-3.

From the amplitude response during the described engine-order crossings it was impossible to determine a significant variation of blade-individual frequencies. At throttled conditions instead, a clear pattern can be identified with both tip-timing and strain gauges. This is presented in Fig. 10 for 80% speed at respective flow rates of 24.3 kg/s, 24.1 kg/s, and 24.3 kg/s, representing the onset of non-synchronous vibrations (NSV) for CATREF, CATMIS, and CATSRT configurations. The graph shows the maximum for each blade as well as the frequencies measured under static conditions (ping-test).

The graphs reveal a noteworthy blade-to-blade variation across all configurations. The Mode-1 pattern exhibits an increased variation under rotation, with deviations surpassing 2%. This observed pattern deviates from the ping test result. Conversely, Mode-2 and Mode-3 almost coincide between static and rotating conditions, both in terms of distribution pattern and maximum amplitude. The peak-to-peak variation under rotation is similar for CATREF, accounting for approximately 80% of the ping-test result for the mistuned cases. This suggests that the intended mistuning pattern can be broadly transferred from static analysis to rotation, particularly for the two torsional eigenmodes considered most susceptible to NSV.

Flexural Mode-1 instead showed high sensitivity to the ping test clamping procedure affecting the non-linear blade-disk connection. As will be shown later, Mode-1 does not develop a coherent interaction Mode during NSV, comparably low amplitudes and a wide peak in the average spectrum (Fig. 12). Due to this incoherence, the subsequent analysis focuses on Mode-2 and Mode-3. It is crucial to note that the robust transfer of the cold-condition to rotation for the flexural Mode is not assured.

In summary, the accurate transfer of cold blade identification of torsional eigenfrequencies from ping tests and tip clearance from 3D scans to the rotating environment was achieved. The small stagger variation pattern in the cold shape (< 0.1 deg) did not manifest under rotation, nor did the mistuning in the first eigenmode. In the CATREF and CATMIS configurations, the unintentional variation of tip clearance was associated with the fabrication process of individual blades. However, the available instrumentation allows for a clear identification of this variation.

Non-synchronous vibration at 80% speed

A systematic investigation of the stability limit was conducted for all presented configurations at constant speedlines. To decrease the mass flow rate, the throttle was incrementally closed in steps of 0.1% of its area, and the machine was stabilized for at least 40 seconds for each measurement point. The experiments were aborted during repeated transient runs when blade vibration amplitudes reached 50% of the Goodman scope limit. Non-synchronous blade vibrations were encountered at all subsonic speedlines and involving all modes. Fig. 11 presents the evolution of amplitude and peak frequency at 80% speed. The shown values were obtained by using a windowed Fourier transformation with a frequency resolution of 0.05 EO (window size 20 revolutions) and subsequently averaging spectra over 40 seconds of operation [24]. Subsequently, a single-degree-of-freedom (SDOF) amplitude response function was employed, and least squares regression was applied to the three eigenmodes. This process facilitated the determination of the peak amplitude ($\hat{\varepsilon}$), resonant frequency (f_i), and modal damping.

Consistently across the tested configurations, a gradual evolution is observed, indicating limit cycle oscillations with peak

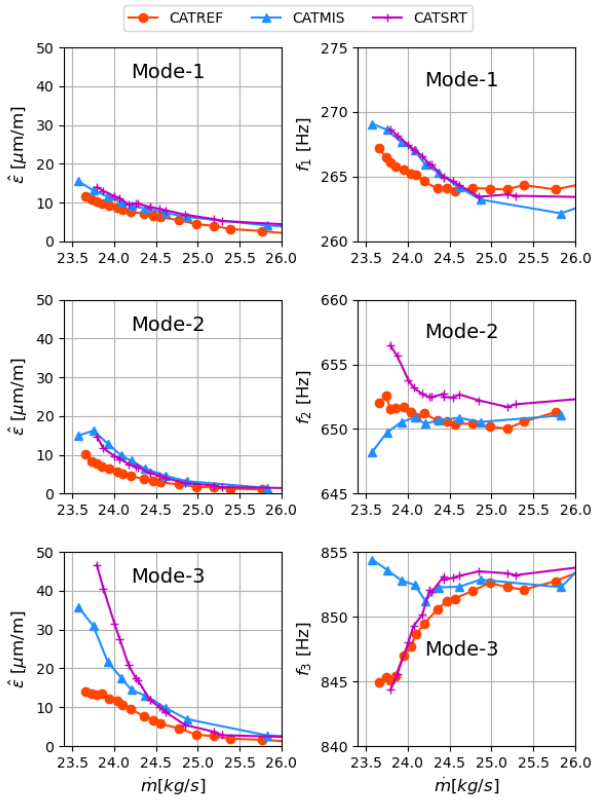

FIGURE 11: Transient evolution of modal amplitude at 80% speed during NSV onset from strain gauges for CATREF, CATMIS and CATSRT configurations.

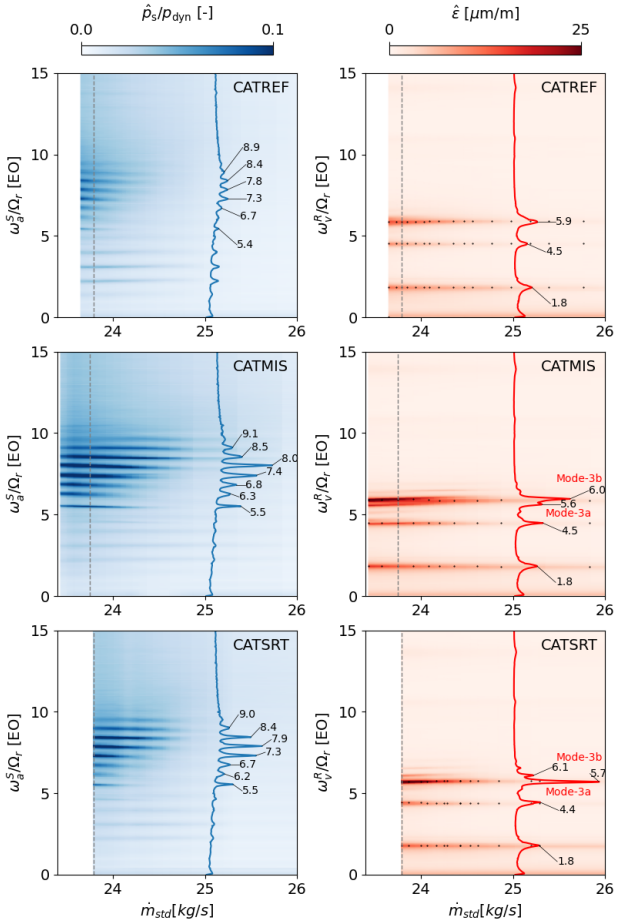

FIGURE 12: Spectral analysis of casing wall pressure near the rotor leading edge and rotor-strain gauge signal during NSV at 80% speed for CATREF (a), CATMIS (b) and CATSRT (c).

amplitude scaling to throttle degree. The evolution of Mode-1 amplitude and frequency is comparable for all configurations with a slight increase of resonant frequency towards lower mass flow.

In contrast, Mode-2 exhibits a distinct amplitude trend, registering a twofold increase for CATMIS/CATSRT in comparison to the reference configuration (CATREF). A significant observation becomes apparent for mass flows below 24 kg/s. While the reference configuration maintains a steady average frequency of 652 Hz, the other configurations deviate: CATMIS experiences a 4 Hz decrease, and CATSRT sees a 5 Hz increase (0.8%). It's important to note that this value is an average across all blades.

For Mode-3, a distinct pattern emerges, where the average amplitude at low mass flow uniformly increases from CATREF through CATMIS to CATSRT. The average frequency evolution is comparable for CATREF and CATSRT, experiencing a decrease of up to 9 Hz (approximately 1%), while CATMIS remains constant.

The graphs intentionally maintain their dimensional representation to underscore the similarity in initial frequency and the divergent, mode-dependent behavior with throttling.

These observations were entirely unforeseen before the experiments. Despite predictions suggesting that all patterns of structural mistuning would be more stable than a perfectly tuned case, the divergent and inconsistent behavior of the mistuned configurations, exhibiting higher vibration amplitudes at similar mass flow for all blade modes, necessitates further analysis.

Unsteady wall static pressure probes and strain gauges are analyzed to identify interaction patterns between aerodynamic disturbances and structural blade vibration modes. Fig. 12 presents the spectrogram of non-synchronous pressure fluctuations and blade strain variations over mass flow rate during NSV at 80% speed for all setups. To isolate non-synchronous signals, a sliding ensemble-average of each 10 revolutions has been subtracted. The spectrograms represent an average from distributed unsteady pressure sensors near the leading edge of the rotor and an average of all strain gauges signals located at the suction side. Note that the pressure signal is in the steady frame of reference, strain gauges in the rotating. All spectrograms result from a series of stabilized operating conditions to avoid transient contributions. Within each map, the spectrum for massflow $\approx$ 23.8kg/s (shown as dashed line) is presented to facilitate the identification of individual frequency peaks. Rotation speed was adapted to conserve Mach-similarity considering inlet temperature and humidity, yielding 8629 rpm for CATREF, 8676 rpm for CATMIS and 8878 rpm for CATSRT.

For all configurations, the well-known broadband disturbance commonly discussed as 'Rotating Instabilities' [27, 28] and centered around half the blade passing frequency (EO8) is present in the pressure spectra. The aerodynamic structure of the disturbances responsible for these signals has been exten-

sively discussed and experimental measurements are provided in [25]. Small scale vortical disturbances develop in the leading edge region near the casing and are convected upstream of the blockage zone towards the trailing blade, impacting near the leading edge. For the CATANA case, simulations illustrating the flow structures at 80% are reported in [13], and with varying tip clearance in [29]. Comparison between configurations shows increased unsteadiness for the both mistuned configurations for comparable conditions. At equal mass flow 23.8kg/s, CATREF shows barely distinguishable peaks, which are almost five times higher for CATMIS and CATSRT. The rake of frequency peaks is comparable between all configurations, centered around EO8 and slightly increasing in frequency towards lower mass flow. As discussed in [30], each peak can be associated to a specific wave number of aerodynamic disturbances, and the changing frequency is associated to a slightly varying propagation speed $\omega_a^S = N_a \Omega_a^S$.

The aerodynamic disturbances observed in the CATREF rotor present a prominent peak at EO7.2, compared to EO8.0 for CATMIS and EO7.9 for CATSRT.

Regarding the averaged vibration spectra, the three first eigenmodes are clearly distinguishable. As shown previously, amplitudes increase continuously towards lower mass flow. For CATREF the modal peaks are symmetric across the the whole investigated range. Same applies to Mode-1 and Mode-2 for all configurations. The spectrograms of CATMIS and CATSRT (b, c) instead indicate a different behavior for Mode-3. In both spectra, two distinct peaks, denoted Mode-3a and Mode-3b, corresponding to EO5.6 and EO6.0 respectively for CATMIS – EO5.7 and EO6.1 for CATSRT are observed with increasing intensity towards low mass flow below 24 kg/s. This observation indicates a systematically different behaviour compared to CATREF. Note that EO6.0 (rotating)/ EO8.0 (stationary) signal in the CATMIS case is not a forced-response issue, the ensemble average has been subtracted, individual peaks from different blades are spread closely around the EO and when changing massflow the values evolve continuously.

To characterize the associated assembly modes, the nodal diameters are derived from rotor strain gauges. In a first step, only assembly modes which are coherent over the whole circumference are analyzed. To achieve this, a band-pass filter was used to isolate individual modes (peak frequency ±0.5EO, -20dB/decade). Then, all possible pairwise cross-correlations between blades are calculated, mapped to circumferential propagation speed according to Eq. 2 and finally the minimum value of each correlation vector plotted in Fig. 13. The detailed procedure, which eliminates aliased peaks and incoherent modes was outlined in [25]. For aerodynamic disturbances, the same procedure is applied but using casing Kulite sensors in the leading edge plane, resulting in the maps shown in Fig. 13(c).

The maps presented in Fig. 13 clearly depict a coherent evolution of distinct nodal diameters for Mode-2 and Mode-3 for the CATREF (a) and CATMIS (b) configurations. At higher massflow a dominant Mode-2 N_v7 is observed, shifting to N_v6 when approaching the stability limit. CATREF shows much lower correlation values but similar wave numbers. For Mode-3, the results differ significantly. CATREF presents a low amplitude N_v3 and N_v2 signal while the mistuned configurations develop highly coherent peaks. CATMIS dominates N_v2 but also comprises significant amplitude of N_v3. Same applies to CATSRT, but with inverse amplitude ratio. Further spectral analysis indicates, that for both configurations the N_v2 signal can be associated to Mode-3b (slightly higher frequency) and the N_v3 pattern to Mode-3a, the associated aerodynamic wave numbers are 13 (N_v3) and 14 (N_v2). For the respective aerodynamic disturbances, a propagation speed of 57% Ω_r is measured independent from the wave number as shown in Fig. 13(c), but again with higher coherence for the two mistuned configurations. Note that this graph is independent from the disturbance amplitude, and hence indicates that the CATREF configuration has the lowest circumferential coherence of disturbances among the tested setups, but a similar average disturbance speed.

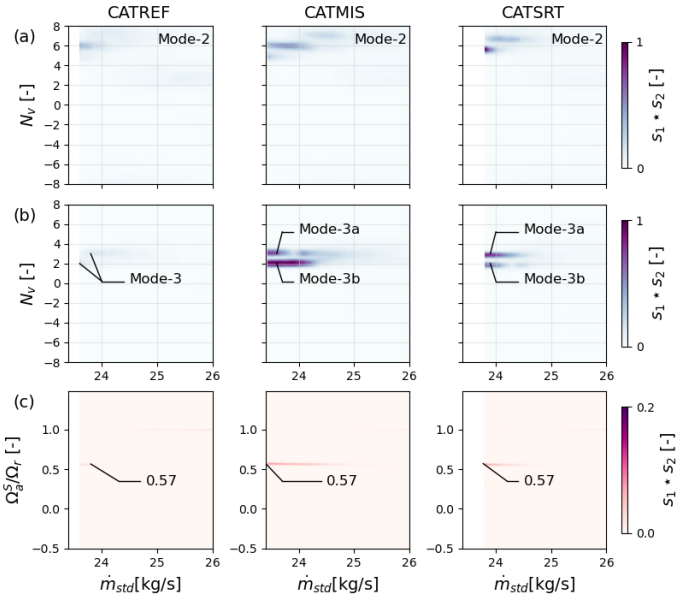

FIGURE 13: Transient evolution of the nodal diameter with massflow from strain gauge cross-correlations for Mode-2 (a) and Mode-3 (b) and transient evolution of group velocity of aerodynamic disturbances (c) during the NSV onset at 80% speed for CATREF, CATMIS and CATSRT rotor configurations.

In this form, such a behaviour was not reported in literature for a high-speed NSV case. The clearly depicted peaks in the pressure spectra indicate stable aerodynamic disturbance patterns with low decay rate. Strong interaction with the blade modes leads to lock-in and associated frequency shift as described in [12], but in the present case, two distinct aerodynamic wave numbers (13 and 14) coexist at high amplitude and force blade vibration of Mode-3 to split. This feature explains the divergent frequency evolution observed in Fig. 11. Mode-3 in the CATMIS case shifts predominantly to Mode-3b (N_v2) with increased frequency, and vice versa for CATSRT. In the CATREF case, the frequency evolution is coincident with the CATSRT configuration, where a dominant Nodal Diameter of 3 (aerodynamic wave number of 13) persists. For Mode-2 no modal splitting is observed but the described forcing mechanism with dominant aerodynamic wave numbers can be drawn to explain the observed behaviour. Obviously, the lock-in behaviour of each

configuration is dominated by aerodynamic forcing with continuously evolving propagation speed and stable disturbance patterns with distinct wave-numbers. Hence, the mechanism has a strong non-synchronous forced response character which indicates that observed vibration amplitudes depend largely on the mechanical speed. For a given wave number the resonance condition is given as:

$$\omega_v^R = N_a \Omega_a^R \text{ where } N_a = \{1, 2, \ldots, n\} \quad (5)$$

As the experiments have been conducted with rotation speed adapted to inlet temperature and humidity in order to match Mach-Numbers, the respective proximity to resonance condition for a specific interaction mode varied between the configurations The mechanical speed of the CATREF measurements was 2.8% lower than of CATSRT. Variation of blade eigenfrequencies ω_v^R with rotation speed is very low, but the fan has a characteristic disturbance speed of $\Omega_a^R/\Omega_r = 0.57$, independent of aerodynamic wave number, hence affecting resonance proximity.

Towards low mass-flow the mechanism can be considered as multi-cell rotating stall forcing the blades with negligible influence of vibration on aerodynamic propagation characteristics. This does not contradict the fact that high amplitude blade vibration enforces the development of distinct wave numbers in the aerodynamic disturbance pattern.

According to this analysis it is difficult to quantify the effectiveness of structural mistuning based on the presented amplitude evolution. Yet, the general trend clearly indicates that for the given case, structural mistuning within the applied range was not beneficial. For the CATMIS and CATSRT case aerodynamic disturbances occurred at higher mass-flow and with higher coherence.

Analysis of system symmetry

This phenomenon is further illustrated in Fig. 14(a, b), depicting the local amplitude of unsteady pressure at the casing for equal mass flow 23.8kg/s between CATREF (a) and CATMIS (b). In this figure, it is clear that the local disturbance maximum observed in the CATREF case is concentrated between blades 15 and 2, situated at approximately the same level as the maximum in the mistuned case.

However, in a wide sector between blades 2 and 6, disturbances are significantly reduced in the CATREF case, while CATMIS displays mostly uniform disturbance amplitudes. To highlight this, the maps shown in Fig. 14(c, d) emphasize the difference to a bladewise mean of these maps, revealing the distinct inhomogeneity present for the CATREF configuration.

To explain this circumferential asymmetry of unsteadiness, a possible factor is the local tip clearance. In the CATREF case, a correlation to the local leading edge clearance presented in Fig. 8 can be observed. Blades 7 to 9 and 14 to 16 represent groups with high tip clearance and can be linked to the areas with high aerodynamic unsteadiness. The same applies conversely, except for individual blades. The strongest decrease of aerodynamic unsteadiness is observed between blades 1 through 3, and these represent a group with low tip clearance at leading edge (Fig. 8).

For the mistuned case no such correlation can be drawn. The variation amplitude of tip clearance is comparable between CATMIS and CATREF, as is the average value. Blade individual

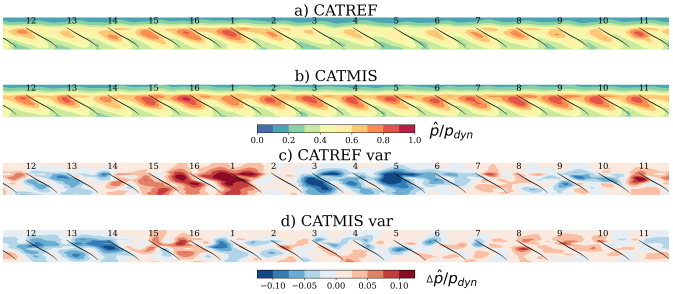

FIGURE 14: Blade-to-blade visualizations of the unsteady wall pressure amplitude at the casing at deep NSV 23.8 kg/s at 80% speed for the CATREF (a) and CATMIS (b) and pressure variation from its respective average passage (c, d) for both configurations.

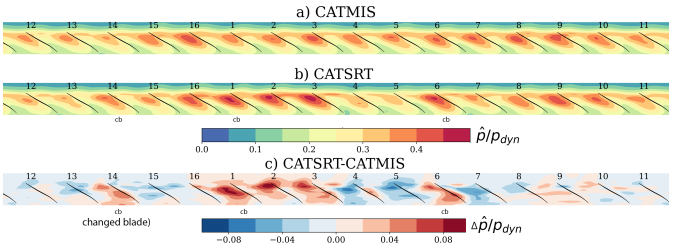

FIGURE 15: Blade-to-blade visualizations of the unsteady wall pressure amplitude at the casing during NSV onset 24.3 kg/s at 80% speed for the CATMIS (a) and CATSRT (b) configurations and pressure differences (c) between both configurations.

stagger angle was neither found to be correlated to the observed asymmetry. Yet, the plot of the tip clearance pattern in Fig. 8 shows that the two mistuned configurations present abrupt and alternating changes, whereas CATREF presents a smooth evolution with wide sectors of similar clearance.

Regarding the direct comparison between the CATMIS and the CATSRT configuration, the maps presented in Fig. 15 are derived, shown for a point with higher mass flow 24.3 kg/s. Here, the CATMIS setup presents a slightly higher asymmetry compared to the map in Fig. 14, but still without clear correlation to tip clearance. However, a more definitive comparison emerges when considering the CATSRT setup. The overall asymmetry pattern aligns between the configurations, but in the vicinity of the changed blades 1, 6, and 14, the pattern is disrupted. Near these blades, aerodynamic unsteadiness increases over a broad range of chord, as highlighted in the map illustrating the difference between the configurations, Fig. 15. Additionally, downstream of Blade 1, heightened unsteadiness is observed in the leading edge plane up to Blade 4.

Considering that all replaced blades introduce a comparable change in tip clearance (Fig. 8), it is evident that the influence on aerodynamic unsteadiness is subtly dependent on this parameter. Rather than being immediatly correlated to individual blade tip clearance, a sectorwise dependency is observed. For the CATREF configuration blade packages of 3-4 blades have comparable clearance and correlations with aerodynamic unsteadiness are evident. In the mistuned configurations, abrupt changes of tip clearance do not show this trend. This indicates a

cumulative dependency with implications on intentional design, requiring delicate consideration of blade positioning with respect to neighboring blades.

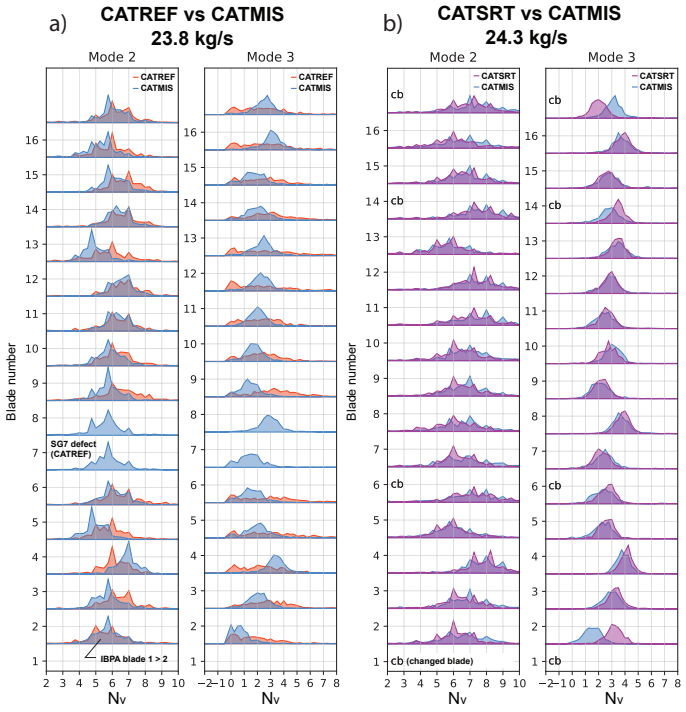

FIGURE 16: Inter-blade phase angle histogram for each blade pair derived from strain gauge data. a) comparison of CATREF and CATMIS at last stable condition CATREF (23.8 kg/s), b) CATSRT vs CATMIS for onset of NSV (24.3 kg/s).

To comprehensively explore the bladewise oscillation behavior, the inter-blade phase angle between adjacent blades was determined using the strain gauges. Temporal signals during stabilized conditions were segmented into windows of 10 revolutions, and the phase between neighboring blades' oscillations was derived through pairwise cross-correlation. Given the temporal variation of the dominant value, a histogram representing occurrence is presented in Fig. 16 (a), illustrating the inter-blade phase angle probability for CATREF and CATMIS for each blade pair. The phase value is normalized by the blade spacing to ensure the same unit as a nodal diameter.

In the case of CATMIS Mode-2, a notable trend towards integer nodal diameter values is evident, such as the consistently dominant N_v6 between blades 6 and 11. This zone also exhibits consistently high unsteadiness in Fig. 14. However, individual blade pairs present different interphase angles, exemplified by N_v7 between blades 3 and 4 or N_v5 for the pair 12-13. In contrast, the CATREF configuration displays wider spread histograms with no distinct switches.

For Mode-3, a slightly different behavior is observed. The respective histograms for the CATMIS case resemble Gaussian distributions but with vastly varying center values, whereas CATREF exhibits wide spreads for each blade and individual peaks at N_v0 (in-phase oscillation).

These results suggest that, for Mode-2 NSV, circumferential coherence of disturbances is more crucial than for Mode-3, given the occurrence of integer nodal diameter values in the histograms for CATMIS and CATSRT configurations. In reduced-order modeling, a similar behavior was noted for very low disturbance decay [31]. Individual blades deviate from the dominant disturbance pattern, with variations exceeding ± 1 N_v.

The observed data challenges the conventional understanding of assembly modes. Assembly modes, or nodal diameter, refer to the collective vibrational behavior of the assembled rotor, considering how individual blades interact to create a coherent response. However, the observed asymmetry in the histograms of inter-blade phase angles, suggests that the concept of an assembly mode does not fully capture the complexity of the system dynamics, and it's significance varies for different modes.

Evidently, significant disturbances of the system resonance are present, more pronounced for the mistuned cases, but their impact on vibration amplitude is complex and generally detrimental.

In the context of a non-synchronous forced response problem with low mistuning, it is proposed that a linear dependency exists between the phase angle and the frequency change between coupled blades. This assumption is particularly evident for Mode-2. Fig. 17 presents a correlation plot between the average Inter-Blade Phase Angle (IBPA) derived from Eq. 4 obtained from the histograms in Fig. 16 and the eigenfrequency difference of each blade pair ($f_{i+1} - f_i$).

For both configurations, the results exhibit consistency, with the highest deviations occurring for blades characterized by a substantial blade-to-blade variation of eigenfrequency. This implies that blades with significant differences in their natural frequencies demonstrate more pronounced shifts in the inter-blade phase angle in response to changes in frequency.

For Mode-3, the correlation trend is unclear for the CATREF configuration. However, in the CATMIS configuration, a correlation is observed, particularly for high-frequency variations. Interestingly, Blade 1 stands out by oscillating widely out of assembly phase, even though the pairwise mistuning is low.

When blade 1 is replaced in the CATSRT configuration, the correlation is reestablished, as illustrated in Fig. 17(b). The accompanying histograms, presented in Fig. 16(b), highlight a drastic phase change in the oscillation of Blade 1 in Mode-3. The oscillation switches from $N_v1.5$ to 3, aligning with the adjacent blades. The other replaced blades (Blades 6 and 14) also induce local changes in oscillation phase, but these changes are much less pronounced than those observed for Blade 1.

Upon revisiting Fig. 15, it was noted that downstream of Blade 1, higher pressure fluctuations were observed, contrasting with Blades 6 and 14. This observation aligns with the presented vibration phase results for Mode-3. In the CATMIS configuration, the local (aerodynamic) mistuning of Blade 1 was high, forcing the blade to oscillate out of assembly phase. Upon replacement, the fan sector from Blade 1 to 4 is compelled into coherent oscillation between N_v2 and N_v3, enabling the gradual growth of aerodynamic disturbances of the corresponding wave number (between 13 and 14). As a result, over the entire sector, aerodynamic unsteadiness in the leading edge region increased (Fig. 15). Although the changed Blade 1 exhibited a significant change in tip clearance, its cold Mode-3 eigenfrequency remained

unchanged (see Fig. 4).

On the contrary, blades 6 and 14 underwent a consistent adjustment in tip clearance, yet their influence on vibration phasing was less pronounced. Their placement within a disk sector exhibiting a low IBPA gradient of Mode 3, as illustrated in Fig. 16, suggests a subtle relationship with eigenfrequency mistuning. The results presented clearly underscore the significance of considering tip clearance in system tuning, particularly when variations are notable, as observed in the studied case.

CONCLUSION

In the exploration of the CATANA/ECL5 open test case, three experimental configurations were examined, each featuring identical blade profiles. The primary focus was on understanding the influence of structural mistuning on Non-Synchronous Vibration (NSV). The study encompassed a predominantly tuned setup, compared with two mistuned configurations characterized by doubled structural eigenfrequency variations.

Static ping-test results were effectively transferred to rotating conditions for torsional modes susceptible to NSV. However, challenges were encountered for the more blade-disk connection-sensitive first flexural mode. 3D-scans of the individual blades transferred well into tip clearance estimations considering FEM simulation results. Manufacturing tolerances introduced low variation in modal eigenfrequencies but high tip clearance variations, prompting further research into their impact.

Structural mistuning significantly influenced vibration phasing, in alignment with low-amplitude mistuning theory. Clear correlations were observed between inter-blade phase angles and frequency differences, suggesting potential stability prediction using reduced-order models.

However, observed modal amplitudes of both mistuned configurations were found to exceed those of the structurally tuned case significantly at similar mass-flow. This stands in contrast to reduced order model predictions considering only structural mistuning. A strong non-synchronous forced response character of the aeroelastic interaction was identified, with a fixed relative disturbance propagation speed, affecting resonance proximity depending on mechanical speed and hence impeding direct quantification of structrual mistuning effectiveness.

Blade-wise analysis highlighted higher asymmetry in coherent aerodynamic disturbances in the reference configuration compared to the mistuned cases. Correlations with tip clearance were identified, emphasizing its impact on blade phasing and disturbance coherence.

The presented results offer insights for coupled simulations with non-symmetric blade geometries. The geometry is available to a wide range of research institutes upon request. Detailed measurements of tip clearance and cold eigenfrequencies can be found in the appendix.

In summary, the results underscore the significant impact of aerodynamic and structural mistuning on NSV. Furthermore, they suggest the potential for system stabilization through intentional design of asymmetry, offering a practical solution for fan assembly in engine production.

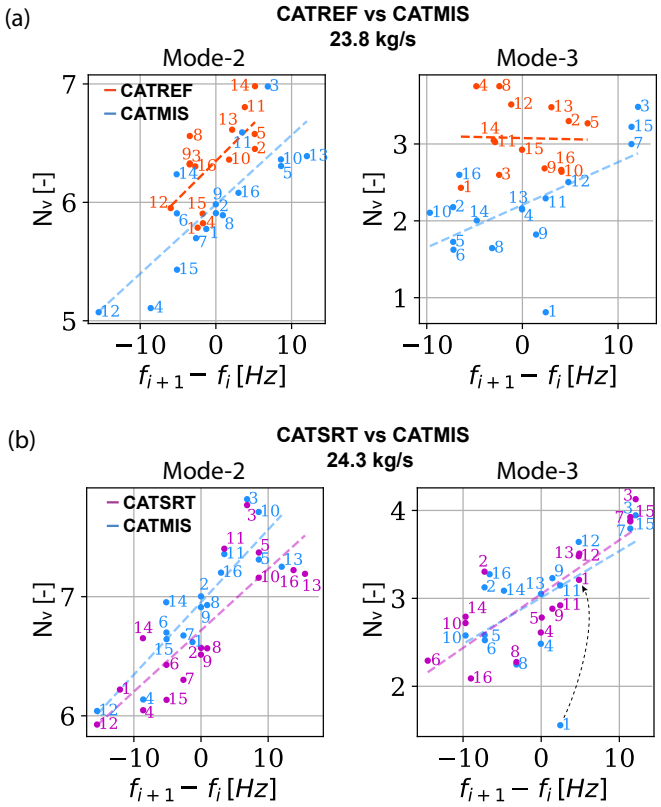

FIGURE 17: Correlation between average interblade phase angle and bladewise eigenfrequency difference (a) 23.8kg/s CATREF vs CATMIS, (b) 24.3kg/s CATMIS vs CATREF

ACKNOWLEDGMENTS

The results presented in this paper rely on the contributions of a large research group and the authors gratefully acknowledge the excellent collaboration and support over the past five years. The authors particularly thank Pavel Teboul, Cedric Desbois, Sebastien Goguey, Gilbert Halter, Lionel Pierrard, Laurent Pouilloux, Edouard Salze of LMFA, Kevin Billon and Claude Gibert of LTDS for their support and contributions to the experiments, Valdo Pages, Stephane Aubert, Pascal Ferrand, Pierre Duquesne and Laurent Blanc during the design of the geometry. The final design was developed in close collaboration with Safran Aircraft Engines, and the authors particularly acknowledge the help of Laurent Jablonski. We are grateful for the continuous collaboration and financial support of SAFRAN Aircraft Engines since the beginning of this project and specifically for the present measurement campaign, for which the test module MARLYSA was provided by SAFRAN. For the tip-timing measurements we received extensive support of Gerhard Ziller, Marco Hermann and Simon Kytzia of MTU Aero Engines.

The reduced order model used to determine stability of the mistuned cases was developed together with Sina Stapelfeldt of Imperial College, and the authors are grateful for the continuous collaboration on methodological development.

The presented research was financed through the European Union's Clean Sky 2 Joint Undertaking (JU) under grant agreement N864719, CATANA. The JU receives support from the

European Union's Horizon 2020 research and innovation program and the Clean Sky 2 JU members other than the Union. The paper reflects only the author's view and the JU is not responsible for any use that may be made of the information it contains. Assessment of the test facility was enabled through financial supports of Agence Nationale de la Recherche (ANR, Project d'EquipEx PHARE) and Conseil pour la Recherche Aeronautique Civile (CORAC - Programme CUMIN). Buildings and infrastructure were supported by ECL, instrumentation supported by Institut Carnot (INGENIERIE@LYON - Project MERIT) and SAFRAN Aircraft Engines.

REFERENCES

[1] Bontemps, Thomas, Aubert, Stephane and De Cacqueray, Nicolas. "Prediction of the acoustic influence of an intake on fan flutter." *13th European Turbomachinery Conference on Turbomachinery Fluid Dynamics and Thermodynamics*. 2019. DOI hal-03855699.

[2] Goessling, Jan, Seume, Joerg R., Flueh, Jan Peter, Paletta, Nicola, Eggers, Torben, Friedrichs, Jens and Natale, Nunzio. "Aerodynamic Damping of Composite UHBR Fans Under the Consideration of Acoustic Intake Reflections.": p. V08AT21A008. 2022. DOI 10.1115/GT2022-81777. URL https://doi.org/10.1115/GT2022-81777.

[3] Hill, George, Gambel, Julian, Schneider, Sabine, Peitsch, Dieter and Stapelfeldt, Sina. "Aeroelastic Stability of Combined Plunge-Pitch Mode Shapes in a Linear Compressor Cascade." *International Journal of Turbomachinery, Propulsion and Power* Vol. 7 No. 1 (2022). DOI 10.3390/ijtpp7010007. URL https://www.mdpi.com/2504-186X/7/1/7.

[4] Lee, Kuen-Bae, Wilson, Mark and Vahdati, Mehdi. "Numerical Study on Aeroelastic Instability for a Low-Speed Fan." *Journal of Turbomachinery* Vol. 139 No. 7 (2017): p. 071004. DOI 10.1115/1.4035569. URL https://asmedigitalcollection.asme.org/turbomachinery/article-pdf/139/7/071004/6306813/turbo_139_07_071004.pdf, URL https://doi.org/10.1115/1.4035569.

[5] Kielb, Robert E., Feiner, Drew M., Griffin, Jerry H. and Miyakozawa, Tomokazu. "Flutter of Mistuned Bladed Disks and Blisks With Aerodynamic and FMM Structural Coupling." Vol. Volume 6: Turbo Expo 2004: pp. 573–579. 2004. DOI 10.1115/GT2004-54315. URL https://doi.org/10.1115/GT2004-54315.

[6] Pinelli, Lorenzo, Arnone, Andrea, Peruzzi, Lorenzo, Bettini, Claudio, Finzel, Conrad and Kellerer, Rudolf. "Mistuning Strategy on Long Blades to Mitigate Flutter.": p. V11AT21A012. 2023. DOI 10.1115/GT2023-102933. URL https://doi.org/10.1115/GT2023-102933.

[7] Kielb, Robert E, Barter, John W, Thomas, Jeffrey P and Hall, Kenneth C. "Blade excitation by aerodynamic instabilities: A compressor blade study." *Turbo Expo: Power for Land, Sea, and Air*, Vol. 36878: pp. 399–406. 2003.

[8] Franke, Daniel, Jüngst, Maximilian, Möller, Daniel, Schiffer, Heinz-Peter and Giersch, Thomas. "Influence of preswirl, rotor speed and blade count on aeroelastic coupling mechanisms during stall inception of a transonic compressor." *Turbo Expo: Power for Land, Sea, and Air*, Vol. 84218: p. V10AT24A015. 2020. American Society of Mechanical Engineers.

[9] Jüngst, Maximilian, Franke, Daniel, Schiffer, Heinz-Peter and Giersch, Thomas. "Aeroelastic effects in a transonic compressor with nonaxisymmetric tip clearance." *Global Power and Propulsion Society Forum*, Vol. 18: pp. 7–9. 2018.

[10] Dodds, J. and Vahdati, M. "Rotating Stall Observations in a High Speed Compressor—Part I: Experimental Study." *J. Turbomach.* Vol. 137 No. 5 (2015): pp. 51002–51010. URL https://doi.org/10.1115/1.4028557.

[11] Zhao, Fanzhou, Dodds, John and Vahdati, Mehdi. "Influence of blade vibration on part-span rotating stall." *International Journal of Gas Turbine, Propulsion and Power Systems* Vol. 12 No. 2 (2021): pp. 1–7.

[12] Stapelfeldt, Sina and Brandstetter, Christoph. "Non-synchronous vibration in axial compressors: Lock-in mechanism and semi-analytical model." *J. Sound and Vibration* Vol. 488 (2020): p. 115649. DOI 10.1016/j.jsv.2020.115649.

[13] Fiquet, Anne-Lise, Ottavy, Xavier and Brandstetter, Christoph. "UHBR Open-Test-Case Fan ECL5/CATANA: Non-linear analysis of non-synchronous blade vibration at part-speed conditions." *16th International Symposium on Unsteady Aerodynamics, Aeroacoustics and Aeroelasticity of Turbomachines, Toledo, Spain, Sept*. 2022. DOI hal-03800486.

[14] Hah, Chunill. "Large eddy simulation of transonic flow field in NASA rotor 37." *47th AIAA Aerospace Sciences Meeting including The New Horizons Forum and Aerospace Exposition*: p. 1061. 2009.

[15] Khaleghi, H, Boroomand, M, Tousi, AM and Teixeira, JA. "Stall inception in a transonic axial fan." *Proceedings of the Institution of Mechanical Engineers, Part A: Journal of Power and Energy* Vol. 222 No. 2 (2008): pp. 199–208.

[16] Klausmann, Fabian, Franke, Daniel, Foret, Jonas and Schiffer, Heinz-Peter. "Transonic compressor Darmstadt - Open test case Introduction of the TUDa open test case." *Journal of the Global Power and Propulsion Society* Vol. 6 (2022): pp. 318–329. DOI 10.33737/jgpps/156120. URL https://doi.org/10.33737/jgpps/156120.

[17] Pages, Valdo, Duquesne, Pierre, Ottavy, Xavier, Ferrand, Pascal, Aubert, Stephane, Blanc, Laurent and Brandstetter, Christoph. "UHBR open-test-case fan ECL5/CATANA, Part 2 : Mechanical and aeroelastic stability analysis." *Proc. 14th European Conference on Turbomachinery Fluid dynamics and Thermodynamics, ETC2021-625*. 2021. DOI hal-03257377.

[18] Fiquet, Anne-Lise, Schneider, Alexandra P., Paoletti, Benoit, Ottavy, Xavier and Brandstetter, Christoph. "Experiments On Tuned UHBR Open-Test-Case Fan ECL5/CATANA: Stability Limit." *J. Eng. Gas Turbines Power.* (2023): pp. 1–12DOI 10.1115/1.4063717.

[19] Pages, Valdo, Duquesne, Pierre, Aubert, Stephane, Blanc, Laurent, Ferrand, Pascal, Ottavy, Xavier and Brandstetter,

Christoph. "UHBR Open-Test-Case Fan ECL5/CATANA." *International Journal of Turbomachinery, Propulsion and Power* Vol. 7 No. 2 (2022). DOI 10.3390/ijtpp7020017.

[20] Stapelfeldt, Sina and Brandstetter, Christoph. "Suppression of Nonsynchronous Vibration Through Intentional Aerodynamic and Structural Mistuning." *J. Turbomach.* Vol. 144 No. 2 (2022). DOI 10.1115/1.4052233.

[21] Brandstetter, Christoph, Pages, Valdo, Duquesne, Pierre, Paoletti, Benoit, Aubert, Stephane and Ottavy, Xavier. "Project PHARE-2 : A High-Speed UHBR Fan Test Facility for a New Open-Test Case." *J. Turbomach.* Vol. 141 No. 10 (2019): p. 101004. DOI 10.1115/1.4043883.

[22] Schneider, Alexandra P., Paoletti, Benoit, Ottavy, Xavier and Brandstetter, Christoph. "Influence of a turbulence control screen on the aerodynamic and aeroelastic behavior of a UHBR fan." 2022. DOI 10.1115/GT2022-81961.

[23] Zielinski, Michael and Ziller, Gerhard. "Noncontact vibration measurements on compressor rotor blades." *Measurement Science and Technology* Vol. 11 (2000): pp. 847 – 856. DOI 10.1088/0957-0233/11/7/301.

[24] Schneider, Alexandra P., Paoletti, Benoit, Ottavy, Xavier and Brandstetter, Christoph. "Experimental monitoring of vibrations and the problem of amplitude quantification." *Journal of Physics: Conference Series* Vol. 2511 No. 1 (2023): p. 012017. DOI 10.1088/1742-6596/2511/1/012017.

[25] Brandstetter, Christoph, Juengst, Maximilian and Schiffer, H.-Peter. "Measurements of Radial Vortices, Spill Forward, and Vortex Breakdown in a Transonic Compressor." *J. Turbomach.* Vol. 140 No. 6 (2018): p. 061004. DOI 10.1115/1.4039053.

[26] Schneider, Alexandra P. "Aerodynamic and Aeroelastic Investigation of a Composite Fan for Ultra-High-Bypass-Ratio Aircraft Engines." Ph.D. Thesis, Ecole de Centrale de Lyon. 2024.

[27] Mailach, Ronald, Lehmann, Ingolf and Vogeler, Konrad. "Rotating Instabilities in an Axial Compressor Originating From the Fluctuating Blade Tip Vortex." *J. Turbomach.* Vol. 123 No. 3 (2001): pp. 453–460. DOI 10.1115/1.1370160.

[28] Pullan, Grahan, Young, Anna, Day, Ivor, Greitzer, Edouard and Spakovszky, Zoltan. "Origins and Structure of Spike-Type Rotating Stall." *J. Turbomach.* Vol. 137 No. 5 (2015): pp. 51007–51011. DOI 10.1115/1.4028494.

[29] Tharreau, Pierre, Hardy-Falch, Magnus, Stapelfeldt, Sina and Brandstetter, Christoph. "Non-synchronous vibration: characterisation of the aerdonyamic disturbance and its dependency on local tip clearance." *To be published GT2024-129186 – Proc. ASME Turbo Expo 2024*. 2024.

[30] Brandstetter, Christoph, Ottavy, Xavier, Paoletti, Benoit and Stapelfeldt, Sina. "Interpretation of stall precursor signatures." *J. Turbomach.* Vol. 143 No. 12 (2021): p. 121011. DOI 10.1115/1.4051709.

[31] Brandstetter, C. and Stapelfeldt, S. "Analysis of a linear model for non-synchronous vibrations near stall." *Int. J. Turbomach., Propulsion and Power* Vol. 6 No. 3 (2021): p. 26. DOI 10.3390/ijtpp6030026.

APPENDIX A. INDIVIDUAL BLADE CHARACTERISTICS FOR CATREF, CATMIS AND CATSRT ROTORS.

(a) Individual blade eigenfrequency from ping-test for CATREF configuration.

Blade n°	Mode-1 f_v [Hz]	Mode-2 f_v [Hz]	Mode-3 f_v [Hz]
1	244	595	842
2	241	593	836
3	243	598	840
4	242	594	838
5	241	593	833
6	243	598	840
7	242	596	838
8	242	599	838
9	244	596	836
10	242	592	838
11	242	594	842
12	242	598	839
13	243	592	838
14	243	594	841
15	243	599	838
16	243	598	838
Mean	**242.54**	**595.55**	**838.37**

(b) Individual blade eigenfrequency from ping-test for CATMIS and CATSRT configurations.

Blade n°	Mode-1 f_v [Hz]	Mode-2 f_v [Hz]	Mode-3 f_v [Hz]
1	243	592	838
1 (CATSRT)	243	603	836
2	239	591	840
3	241	591	833
4	241	598	845
5	243	589	845
6	241	598	838
6 (CATSRT)	243	598	845
7	241	593	831
8	240	590	842
9	241	591	839
10	240	591	840
11	242	599	831
12	242	603	833
13	241	587	838
14	242	599	838
14 (CATSRT)	246	603	843
15	241	594	833
16	240	589	845
Mean	**241.04**	**593.40**	**838.08**
Mean (CATSRT)	**241.43**	**594.29**	**838.69**

TABLE 2: Individual blade tip clearance (leading edge LE – mid-chord MC – trailing edge TE) at PE at 100% of design speed for the CATREF, CATMIS, and CATSRT configurations.

Blade n°	CATREF			CATMIS			CATSRT		
	LE	MC	TE	LE	MC	TE	LE	MC	TE
$\bar{t}$ [mm]	0.913	0.808	0.890	1.043	0.818	0.860	1.153	0.894	0.935
1	-0.009	0.034	0.035	-0.033	0.006	0.059	0.127	0.059	0.005
2	-0.074	-0.039	0.002	-0.033	-0.043	-0.062	-0.073	-0.058	-0.052
3	-0.082	-0.033	-0.056	0.072	0.009	-0.043	0.037	-0.018	-0.050
4	0.033	-0.056	-0.057	0.057	0.013	-0.023	0.022	-0.021	-0.038
5	-0.091	-0.061	-0.037	-0.112	0.001	0.117	-0.154	-0.037	0.091
6	-0.062	0.001	0.017	0.052	-0.027	-0.079	0.177	0.066	-0.075
7	0.016	-0.001	0.032	0.047	0.016	-0.029	-0.003	-0.021	-0.045
8	0.084	-0.012	-0.081	-0.084	-0.030	0.082	-0.134	-0.069	0.059
9	0.003	0.043	0.010	-0.003	0.013	0.001	-0.043	-0.016	-0.011
10	-0.082	-0.066	-0.009	-0.044	-0.035	0.013	-0.073	-0.067	-0.009
11	0.058	0.002	-0.068	0.027	0.014	0.001	-0.003	-0.005	-0.002
12	0.090	0.034	0.008	0.132	0.048	-0.022	0.097	0.028	-0.019
13	-0.053	0.032	0.180	-0.053	0.036	0.059	-0.063	0.017	0.050
14	0.083	0.064	-0.018	0.067	0.006	-0.023	0.227	0.191	0.135
15	0.064	0.056	0.045	-0.003	-0.050	-0.116	-0.028	-0.057	-0.095
16	0.024	0.001	0.000	-0.086	0.025	0.063	-0.108	0.008	0.059

The presented research was supported through Clean Sky 2 Joint Undertaking (JU), project CATANA under grant agreement N◦864719. The JU receives support from the European Union's Horizon 2020 research and innovation programme and the Clean Sky 2 JU members other than the Union. This publication reflects only the author's view and the JU is not responsible for any use that may be made of the information it contains.

catana.ec-lyon.fr
Christoph.brandstetter@ec-lyon.fr